DTU Library

Surface Wetting in Multiphase Pipe-Flow

Bentzon, Jakob Roar; Vural, Attila ; Feilberg, Karen Louise; Walther, Jens Honore

Surface Wetting in Multiphase Pipe-Flow

Jakob Roar Bentzon [1,*], Attila Vural [1], Karen Louise Feilberg [2], Jens Honore Walther [1,3]

[1] Department of Mechanical Engineering, Technical University of Denmark

[2] The Danish Hydrocarbon Research and Technology Centre, Technical University of Denmark

[3] Computational Science and Engineering Laboratory, ETH, Zürich, Switzerland

[*] Nils Koppels Allé, Building 404, Kgs. Lyngby, 2800, Denmark

[*]jroben@mek.dtu.dk

Keywords: Industrial Application, Surface Wetting, Liquid holdup, Eulerian-Eulerian, Corrosion, Scale

Abstract

The present study examines the quantity of surface wetting in a two-phase oil and water pipe flow. The study is performed by employing an Eulerian-Eulerian CFD model using the S-gamma droplet size distribution model within Star–CCM+. In the North Sea production of oil and gas, water-phase surface processes such as scale and corrosion account for more than 40–50 % of operating expenses. The objective of the model is to investigate best practices for the prediction of phase distribution aimed at evaluating the degree of the wall in contact with the water phase (water-wetting). The model is validated by performing detailed numerical simulations corresponding to the experimental studies by Kumara et al. (2009). The comparison yields good agreement with the observed measurements with slight over-prediction of the dispersion rate but accurately describing liquid holdup. The surface wetting is then evaluated with its interdependence with liquid holdup and dispersion rate.

1 Introduction

Flow assurance is a major challenge in the oil and gas industries and amounts to 40–50 % and more of the total operating expenses in many wells due to costly mechanical and chemical intervention. The presence of hard and soft scales (e.g. $CaCO_3$, $BaSO_4$, $FeCO_3$, FeS) might lead to loss of production due to scale build-up and Enhanced corrosion rates due to galvanic effects and fouling of equipment, which can lower the production rates and ultimately render oil-wells unrecoverable. Consequently, it is of major importance to understand the mechanisms and the rates of corrosion and scale deposition under hydrodynamic conditions and realistic flow in the production wells.

Understanding the proportion of wall in contact with the water phase, a property known as water-wetting, is crucial for the development and analysis of mitigation measures. The flow-regime varies from stratified to fully dispersed throughout the well, therefore a fully qualified model should capture the physics of both flow-regimes. The application of the Volume-of-Fluid (VOF) approach to model dispersion of the phases requires interface resolution of the droplets in the flow (Hirt and Nichols 1981). The average droplet sizes in fully dispersed flows are estimated to be in the order of 1 mm through empirical correlations (Schümann et al. 2015) using the maximum diameter observed in experiments by Elseth (2001). This makes the use of the VOF model infeasible for the dispersed flow-regime. In contrast, the Eulerian-Eulerian two-equation approach allows for sub-grid, droplet-dispersion modelling through empirical closure laws and is used throughout this work. This method has been used successfully for a number of liquid-liquid or liquid-gas flows (Prosperetti and Tryggvason 2007)

Attempts to simulate the flow by Kumara et al. (2008), using the VOF approach shows good prediction of the velocity profiles and pressures, but does not describe the dispersion of the phases. An Eulerian-Eulerian approach using droplet sizes determined from the correlations by Brauner (2001) has been studied by Pouraria et al. (2016) to replicate the results from Elseth (2001) and has achieved fairly good agreement. The accuracy of the Eulerian-Eulerian approach depends on the models for determining the transfer of momentum between the phases. Typically, this included drag, lift, surface tension, virtual mass and surface contact forces. These models depend on an estimate of the droplet size. Modelling attempts with a constant droplet size have proven to have limited success in predicting dispersion adequately. Consequently, the S-gamma droplet size distribution model described in (Lo and Zhang 2009) is used in the present study.

From the aforementioned work it is clear that the Eulerian-Eulerian model has good potential as a tool for studies of two-phase flow in oil wells. Thus, a thorough study to validate the model and its parameters is essential for further research. The objective of the present study is to validate and optimize the numerical procedure for two-phase oil and water pipe flows against the experiments from (Elseth 2001) and (Kumara et al. 2009).

To analyse surface wetting, the consequence of liquid holdup, i.e. flow properties causing one fluid to move slower than the other and thereby increasing it's share of cross-

sectional area in the pipe is analysed. Additionally, the rate of dispersion affects how much of each phase is in contact with the wall. Using a validated model, these two phenomena can be analysed for different flow properties.

2 Methodology

A numerical CFD model is set up in Star–CCM+ version 13.04 to investigate the best modelling settings for replicating the experimental study described in (Elseth 2001) and (Kumara et al. 2009). The test rig consists of a pipe-section with diameter $0.0563\,\text{m}$ and length $12\,\text{m}$ (213 diameters), followed by a test section where a time-averaged gamma densitometry measurement was taken across a set of cords in the horizontal direction. The pipe section is preceded by a Y-junction from which oil and water flows into each inlet. The flow is controlled by the flow rate of each phase and reported in terms of mean velocity U (total flow rate divided by cross-sectional area) and water-cut (ratio between flow rate of water and total flow rate).

2.1 Governing equations

The numerical simulations are based on the Eulerian-Eulerian two-fluid approach. This treats both phases as a continuous phase, each with its own velocity field but with a shared pressure field p (Ishii and Hibiki 2006). The fluids are considered isothermal, immiscible and incompressible. Hence, only mass and momentum conservation is considered. Both equations are averaged with a Reynolds decomposition to obtain a solution for the mean flow $\mathbf{u}_k$. This gives a set of volume-fraction-averaged Reynolds Averaged Navier Stokes (RANS) equations for each of the two phases (k =water, oil):

$$\frac{\partial \alpha_k}{\partial t} + \nabla \cdot (\alpha_k \mathbf{u}_k) = 0 \tag{1}$$

$$\frac{\partial \alpha_k \rho_k \mathbf{u}_k}{\partial t} + \nabla \cdot (\rho_k \alpha_k \mathbf{u}_k \mathbf{u}_k) = -\alpha_k \nabla p$$
$$+\alpha_k \rho_k \mathbf{g} + \nabla \cdot \left(\alpha_k \mu_{k,eff} \left(\nabla \mathbf{u}_k + (\nabla \mathbf{u}_k)^T \right) \right) + \mathbf{M}_k \tag{2}$$

where ρ_k and α_k are the density and volume fraction of the k'th phase, $\mathbf{g}$ is the gravitational vector set to $\mathbf{g} = (-9.82 \sin \beta, -9.82 \cos \beta, 0)\,\text{m/s}^2$, where β is the inclination angle of the pipe. $\mu_{k,eff} = \mu_k + \mu_{k,t}$ is the effective dynamic viscosity composed of the dynamic viscosity of the fluid (μ_k) and the turbulent viscosity ($\mu_{k,t}$) from the RANS decomposition Ishii and Hibiki (2006). A Realizable k-ϵ model is used to determine the turbulent viscosity (Shih et al. 1995). All model parameters are left as per Star–CCM+ defaults. The term $\mathbf{M}_k$ corresponds to the exchange of momentum between the two phases. The interfacial momentum transfer forces considered are drag, lift, turbulent dispersion and surface tension. Hence, the $\mathbf{M}_k$ term is subdivided into four closure terms:

$$\mathbf{M}_k = \mathbf{M}_{D,k} + \mathbf{M}_{L,k} + \mathbf{M}_{T,k} + \mathbf{M}_{S,k} \tag{3}$$

where the drag force $\mathbf{M}_{D,k}$, the lift force $\mathbf{M}_{L,k}$, the turbulent dispersion force $\mathbf{M}_{T,k}$ and the surface tension $\mathbf{M}_{S,k}$ are modelled using empirical closure laws.

2.2 Drag force

The drag force is modelled in three different regimes based on the volume fraction of water α_w. The two primary regimes are namely the Dw/o (dispersed water-in-oil) for $\alpha_w < 0.3$, the Do/w (Dispersed oil-in-water) for $\alpha_w > 0.7$. In the intermediate range a blending of the two primary regimes based on the volume fraction is used:

$$\mathbf{M}_{D,k} = \begin{cases} \mathbf{F}_{D,w/o} & \alpha_w < 0.3 \\ \mathbf{F}_{D,o/w} & \alpha_w > 0.7 \\ \alpha_w \mathbf{F}_{D,o/w} + \alpha_o \mathbf{F}_{D,w/o} & \alpha_w \in [0.3, 0.7] \end{cases} \tag{4}$$

$\mathbf{F}_{D,d/c}$ is the drag force of a dispersed droplet of phase d in the continuous phase c and is computed as:

$$\mathbf{F}_{D,d/c} = \frac{1}{2} \rho_p C_D |\mathbf{u}_d - \mathbf{u}_c| (\mathbf{u}_d - \mathbf{u}_c) \frac{A_d}{4} \tag{5}$$

The drag coefficient in the Dw/o and Do/w regimes are computed using the Schiller-Naumann model (Schiller and Naumann 1933):

$$C_D = \begin{cases} \dfrac{24(1 + 0.15 \text{Re}_D^{0.687})}{\text{Re}_D} & \text{Re}_D \leq 1000 \\ 0.44 & \text{Re}_D > 1000 \end{cases} \tag{6}$$

The droplet's Reynolds number Re_D is defined as:

$$\text{Re}_D = \frac{\rho_k |\mathbf{u}_j - \mathbf{u}_d| d_{32}}{\mu_k} \tag{7}$$

where d refers to the dispersed phase (water for Dw/o and oil for Do/w) and c the continuous phase, d_{32} is the Sauter mean diameter of the droplets described in Schümann et al. (2015) and Lo and Zhang (2009).

2.3 Lift force

As a dispersed droplet moves relative to a shear flow it will experience a force perpendicular to the relative velocity proportional to the curl of the continuous phase velocity. This will act to

$$\mathbf{F}_{L_ij} = -C_L \rho_i \alpha_i (\mathbf{u}_i - \mathbf{u_j}) \times (\nabla \times \mathbf{u}_i) \tag{8}$$

where the lift force coefficient C_D is set to a constant of 0.25. As with the drag force, the lift forces are divided into three flow regimes and equation (4) provides the relationship between the flow-regime lift forces and the interfacial lift forces $\mathbf{M}_{L,k}$.

2.4 Turbulent dispersion force

When applying the Reynolds averaging to the drag term, the non-linear term gives rise to an extra turbulent dispersion term. This can be modelled as a dispersion drag coefficient C_{TD} on a turbulent dispersion velocity $\mathbf{u}_{TD}$.

$$\mathbf{M}_T = C_{TD}\mathbf{u}_{TD} \tag{9}$$

The turbulent dispersion velocity has its origin in the phase and Reynolds averaging and is approximated through the Boussinesq closure to:

$$\mathbf{u}_{TD} \approx -\frac{\mu_{c,t}}{\rho_c \sigma_\alpha}\left(\frac{\nabla \alpha_c}{\alpha_c} - \frac{\nabla \alpha_d}{\alpha_d}\right) \tag{10}$$

where α_c, α_d are the Reynolds averaged volume fractions of the continuous and dispersed phase, σ_α is the a coefficient describing the ratio of turbulent dispersion of volume fraction to that of momentum and is set to unity in this work, $\mu_{c,t}$ is the turbulent dynamic viscosity $\mu_{c,t}$ obtained from the k-ϵ model.

The turbulent dispersion drag coefficient is defined from a Stokesian drag coefficient and linearised with the relative velocity of the two averaged phases.

$$C_{TD} = \frac{A_{cd}}{8}\rho_c C_D|\mathbf{u}_c - \mathbf{u_d}| \tag{11}$$

where A_{CD} is the mean interfacial area obtained from the droplet size distribution described in section 2.6. The droplet drag coefficient C_D is modelled as described in section 2.2.

2.5 Surface tension force

The Eulerian-Eulerian two-fluid model does not explicitly track the interface between the phases. To account for surface tension in the physical interface on larger fluid structures, the continuum surface tension model proposed by (Brackbill et al. 1992) and described for a Eulerian-Eulerian two-fluid by (Strubelj et al. 2009) is used. The numerical procedure is to reconstruct the surface normal based on one of the phases $\mathbf{n}_p$ and curvature κ_p

$$\mathbf{n}_p = \frac{\nabla \alpha_p}{|\nabla \alpha_p|} \tag{12}$$

$$\kappa_p = -\nabla \cdot \mathbf{n}_p \tag{13}$$

Based on the curvature the surface tension force in the interface becomes

$$\mathbf{F}_S = \sigma \kappa_p \nabla \alpha_p \tag{14}$$

where σ is the surface tension in units force per length. The force is split between the two phases by dividing the force in the momentum equations relative to the local volume fraction:

$$\mathbf{F}_{S,k} = \alpha_k \mathbf{F}_S \tag{15}$$

To simulate the interaction of the interface at the wall, the wall wetting contact angle θ_w is implemented by defining the interface normal vector of the first computational cell as a transformation of the unit normal vector of the wall $\mathbf{n}_w$ and tangential vector $\mathbf{t}_w$:

$$\mathbf{n}_k = \mathbf{n}_w \cos\theta_w + \mathbf{t}_w \sin\theta_w \tag{16}$$

With limited fluid properties available for the given mixture of water and oil, the wetting angle θ_w is set to $41°$ based

on measurements of deacidified deasphaltened crude oil on stainless steel surfaces in a pure water solution by dos Santos et al. (2006).

2.6 Droplet size

A key to modelling the closure forces is correct estimation of droplet sizes and area density. For this purpose the model employs the S-gamma statistical droplet size distribution model developed by Lo and Zhang (2009) and available in Star–CCM+. The S-gamma model describes the particles through three momentums S_γ where $\gamma \in 0, 2, 3$. Numerically, the model solves for the 2nd moment, S_2, which describes the interfacial area density and optionally it can additionally solve for the zeroth moment, S_0, describing the particle number density. The third moment, S_3, describes the volume density of the droplets and is thus directly correlated to the volume fraction of the dispersed phase:

$$S_{3,k} = \frac{6}{\pi}\alpha_k \tag{17}$$

In this study, only the second moment is used and modelled for both phases. The second moment is formulated as the integral over the droplet size distribution of the square of the diameter and hence represents the average droplet area (A_{CD}) divided by π:

$$S_2 = \int d_p^2 n(d_p)d(d_p) = \frac{A_{CD}}{\pi} \tag{18}$$

By assuming spherical droplets, the Sauter mean diameter, d_{32}, can be calculated as

$$d_{32,k} = \frac{S_{3,k}}{S_{2,k}} \tag{19}$$

The S_γ moments are modelled as convective scalars tracked with a scalar transport equation

$$\frac{\partial S_{\gamma,k}}{\partial t} + \nabla \cdot (S_{\gamma,k}\mathbf{u}_k) = s_{br,k} + s_{cl_k} \tag{20}$$

The source terms $s_{br,k}$ and $s_{cl,k}$ models breakup and coalescence through empirical models described in Lo and Zhang (2009). The critical Weber number used in these models is set to 0.25 for both phases.

To ensure a stable simulation the droplets are initially modelled empirically. Here, a model by Brauner (2001) is employed to estimate the maximum droplet diameter:

$$\frac{d_{max}}{D} = 7.61\text{We}_c^{-0.6}\text{Re}_c^{0.08}\left(\frac{\alpha_d}{\alpha_c}\right)^{0.6}\left(1 + \frac{\rho_d}{\rho_c}\frac{\alpha_d}{\alpha_c}\right)^{-0.4} \tag{21}$$

where We_c and Re_c are the Weber and Reynolds number (see Eq. (26) and (23)) using the velocity, density, and viscosity of the continuous phase. The link between the max diameter and the Sauter mean diameter is estimated by the empirically determined ratio of from Angeli and Hewitt (2000)

$$d_{32} = 0.48\, d_{max} \tag{22}$$

3

2.7 Boundary and initial conditions

The domain boundary is divided into two inlets, a symmetry plane, a wall and an outlet. The inlets are given Dirichlet boundary conditions with prescribed phase-velocities $\mathbf{u}_k$, volume fraction α_k, droplet sizes $d_{32,k}$, turbulent intensity I_k and viscosity ratio $\mu_{k,t}/\mu_k$. The pressure is extrapolated from the domain through reconstruction gradients. The inlet droplet sizes are set to 1mm, the turbulent intensity to 0.01 and the viscosity ratio to 10 as per StarCCM+ defaults.

The outlet is modelled using a homogeneous Neumann condition on all parameters except pressure which is extrapolated in the same way as on the inlet boundary.

Symmetry in the plane spanned by the gravitational vector and the pipe's axial direction is exploited by a symmetry boundary condition (homogeneous Dirichlet on the normal component of the flow, extrapolated pressure and homogeneous Neumann condition on the normal derivatives of all other fields).

The walls are modelled as no-slip walls with homogeneous Dirichlet conditions on the velocity field. The turbulence is modelled using a high y^+ wall treatment model as the wall boundary layer is not sought resolved (Shih et al. 1995).
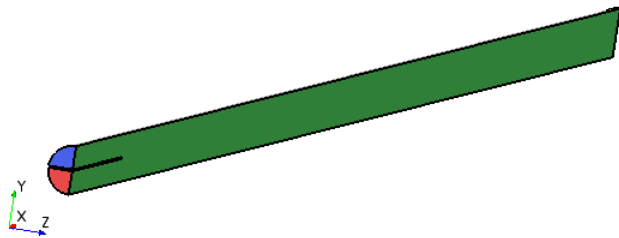

Figure 1: Illustration of the computational domain seen from the inlets. The blue boundary is the inlet of oil, the red the inlet of water. The green boundary is the symmetry plane.

2.8 Numerical solution procedure

The procedure of obtaining a numerical solution to the two-fluid model is parted into three steps for the sake of numerical stability and convergence. Initially, a steady-state version of Equation (1) and (2) is solved by setting the time derivatives to zero. This has not proven numerically stable along with the droplet size distribution model, and is instead carried out with a static constant droplet size determined by Equation (21). The steady-state analysis is run for 1000 iterations. Subsequently, the simulation is switched to a transient analysis. Here the S-gamma droplet size distribution is solved for passively, i.e. without coupling the resulting droplet size to the terms for the momentum equation. This second step is solved with a Courant number of 5 and 40 inner iteration for a physical time of $t = 0.75L_p/U$ where L_p is the modelled length of pipe. seconds of physical time. Finally, the droplet sizes used in the momentum equation is coupled to the S-gamma model and solved for another $t = 0.75L_p/U$ of physical time with a Courant number of 0.1 and a time-step convergence tolerance of 10^{-6} on all equation residuals.

The domain is presented in a Cartesian coordinate system with origo at the mixing point of the incoming flows, the x-axis following the pipe's axial direction, the z-axis horizontal in the gravitational field, with the y-axis following the pipe, aligned with gravity for the horizontal pipe. The computational domain is discretized by a rectangular "trimmer" mesh-grid, with cells in the axial direction of the pipe twice as long as in the radial. The grid sizing is controlled with a single non-dimensional parameter $\hat{\delta}$. The cells located in the core of the domain is set to size $\delta = \hat{\delta}D$ where D is the diameter of the pipe. The traverse directions are refined to 0.25δ and the boundaries are kept as quadratic with a max cell-to-cell stretch of 2. This gives a mesh as shown in Figure 2.
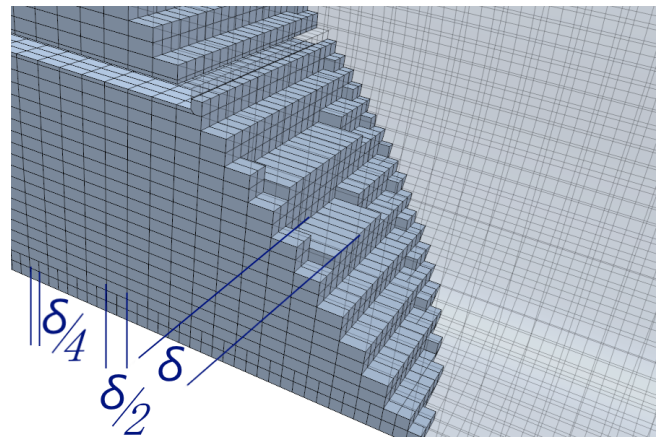

Figure 2: Illustration of the three different sizes in the grid. Picture extracted at the mixing point seen from the symmetry plane and the grid cut through at a $45°$ angle through origo to reveal the interior of the domain.

The computational domain corresponding to the full experimental set-up is computationally expensive to run. Therefore, a study is carried out to evaluate the necessary length of pipe needed for the phase distribution to have reached a constant state.

2.9 Flow conditions

The physics describing the model shows the complex array of parameters affecting the flow. The parameters of the validation are described in Table 1. To simplify the variation study, flow parameters are described in terms of non-dimensionalized numbers, namely the Reynolds (Re), Atwood (A), Froude (Fr) and Weber (We) numbers. The Reynolds number gives the ratio of inertial forces to viscous and is a good indication for the turbulence of the flow, a phase averaged density, ρ_m, and viscosity, μ_m, is used.

$$\mathrm{Re} = \frac{\rho_m U D}{\mu_m} \tag{23}$$

The Atwood number describes the ratio of the difference in density to the average density and is often used to determine instabilities in two-phase flows (Taylor 1950; Glimm et al. 2001).

$$A = \frac{\rho_w - \rho_o}{\rho_w + \rho_o} \tag{24}$$

The effect of gravity is typically described through the Froude number which relates gravity to inertial forces.

$$Fr = \frac{U}{\sqrt{|\mathbf{g}|D}} \tag{25}$$

Finally the relationship between inertia and surface tension is described through the Weber number.

$$We = \frac{\rho_m U^2 D}{\sigma} \tag{26}$$

The water cut ψ is defined as:

$$\psi = \frac{\dot{V}_w}{\dot{V}_w + \dot{V}_o} \tag{27}$$

where $\dot{V}_k$ is the inlet volume flow of phase k.

Parameter	Value
Pipe diameter, D	$0.0563\,\mathrm{m}$
Oil density, ρ_o	$790\,\mathrm{kg/m^3}$
Oil Viscosity, μ_o	$0.00164\,\mathrm{Pa\,s}$
Water density, ρ_w	$1000\,\mathrm{kg/m^3}$
Water Viscosity, μ_w	$0.00102\,\mathrm{Pa\,s}$
Surface Tension, σ	$0.043\,\mathrm{N/m}$
Wetting Contact Angle, θ_w	$41°$

Table 1: Table of parameters from the experimental reference study (Elseth 2001; Kumara et al. 2009). Wetting Contact Angle estimated from dos Santos et al. (2006).

2.10 Validation analysis

The validation is carried out by comparing the densitometry measurements presented by Kumara et al. (2009) to the post-processed Reynolds averaged numerical results. The post-processing takes the cross-sectional volume fraction average it in the z-direction to replicate the density line measurements of the densitometry. The data is presented on a plot with the average volume fraction on the horizontal axis and the radius-normalised y-position on the vertical axis. From this plot, the level of dispersion and liquid holdup can be evaluated as described in Section 2.11. An example of such a cross-sectional volume fraction density plot can be seen in Figure 3.

2.11 Velocity, pressure and liquid holdup

In a horizontal steady flow, a simple force consideration on the two fluids is employed in the x-direction; each phase has pressure gradient, viscous forces and interfacial forces acting on it. The interfacial forces exerted are Newton's third law pairs. Given a fixed pressure gradient, the location of the interface is controlled by a force balance of the viscous and pressure gradient. For identical viscosities, the solution would tend to equal the inflow ratio, such that the area integral of α_w over a cross-section would equal the water-cut. As
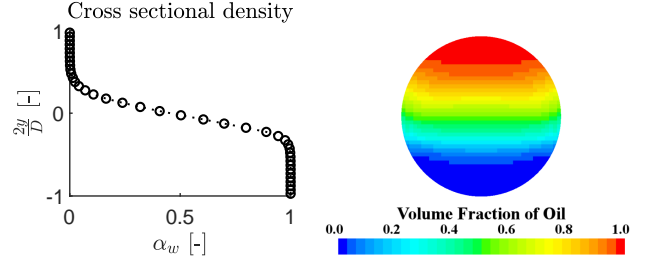

Figure 3: Post-processing illustration of cross sectional volume fraction density on the left and the corresponding phase distribution on the right.

the viscosities differ, the interface moves and one face moves slower relative to the other. This difference in velocity gives rise liquid holdup, i.e. the phase volume ratio in the pipe of each phase is not equal to the water-cut. With the higher viscosity of the oil, a higher holdup of oil is expected. As the pipe is inclined (with the flow moving upwards), gravity acts stronger on the denser fluid and higher holdup of water is expected. The holdup of water increases water-wetting in the pipe and thus costly surface processes. On the phase distribution plots, liquid holdup is indicated by the area under the curve differing from the water-cut. The rate of dispersion is indicated by the slope of the curve. The liquid holdup of water, y_w, is post-processed as the volume integral of the volume fraction of water divided by the total volume V_T in a given section of the pipe:

$$y_w = \frac{1}{V_T} \int_{V_T} \alpha_w dV \tag{28}$$

2.12 Surface Wetting

The numerical model implemented solves for averaged flow quantities, due to the Reynolds averaging as well as the Eulerian description of the phase distribution in each computational cell. Consequently, an assumption is taken to provide a description of the wetting of the walls. In this study, the water-wetting of the wall, W_w, is assumed equal to the surface integral of the extrapolated water volume fraction from the adjacent cells, $\alpha_{w,wall}$ divided by the total area of the wall A_{wall}:

$$W_w = \frac{1}{A_{wall}} \int_{A_{wall}} \alpha_{w,wall} dA \tag{29}$$

This assumes the wetting to be independent on the expected underlying flow pattern (e.g. water droplets dispersed in oil).

3 Results and Discussion

This study describes the validation of the present CFD model against experimental data from Kumara et al. (2009) and an analysis based on the validated model with purpose of understanding how water-wetting of the surface is controlled by flow properties. The flow cases used for validation are listed in Table 2.

Case	Re	A	Fr	We
(0°, 1.0 m/s, 50 %)	37684	0.117	1.348	1166
(5°, 1.0 m/s, 50 %)	37684	0.117	1.348	1166
(0°, 1.5 m/s, 50 %)	56526	0.117	2.023	2623
(0°, 1.5 m/s, 75 %)	67736	0.117	2.023	2776

Table 2: Input condition for the different case studies in the validation analysis. Case name described as (Inclination, Mean velocity, Water-cut)
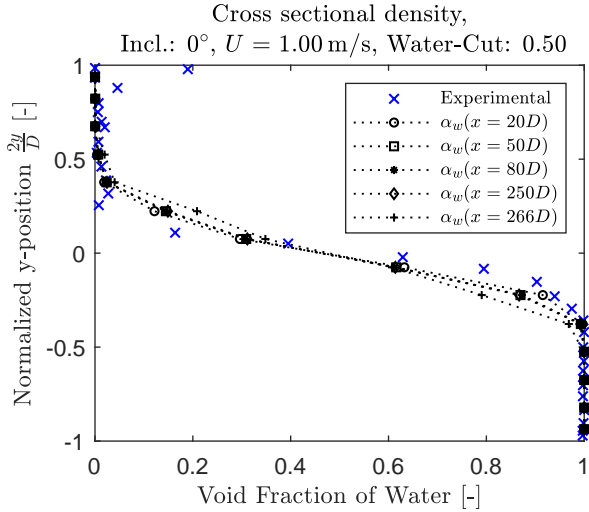

Figure 4: Comparison of phase distribution at different cross sections. Experimental reference by (Kumara et al. 2009).

3.1 Pipe length independence study

A study of the pipe length for the CFD model required to converge to a constant phase distribution profile is performed to reduce the number of computational cells used in the convergence and variation studies. The results from Kumara et al. (2009) are used as reference. The study was performed on a medium-fine mesh of grid size $\hat{\delta} = 0.15$. An extract of the results at different x-positions is shown in Figure 4.

It is observed that while the results, using an intermediate grid-size $d\hat{e}lta = 0.15$, do not converge to the experimental observations, they do stabilize from around 50 diameters downstream until approximately 15 diameters before the outlet where the profile evolves leading up to the boundary. The behaviour is plotted in Figure 5 as RMS error with the mean of results between $x = 240D$ and $x = 250D$ as reference. The distance affected by the outlet has been studied at different flow conditions and seems to remain at 10-15 diameters.

In the remainder of this work, a 75 diameters pipe length is used with sampling at $x = 55D$. Another study was performed for the necessary pipe length preceding the mixing point in order for the velocity profile to develop. Here 15 diameters was concluded to be sufficient length preceding the mixing point. It is noted that "waves" in the RMS occur in the earlier section of the pipe with a wavelength of approximately 5-6 diameters. To average these the results are time-averaged over an timespan based on wave period assuming
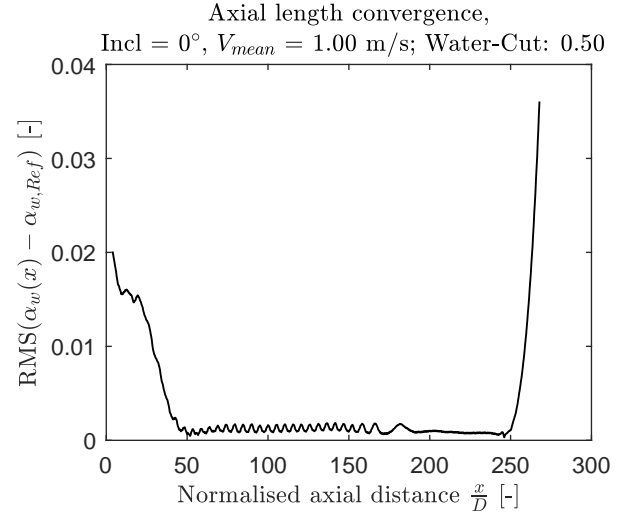

Figure 5: Change in $\mathrm{RMS}(\alpha_w(x) - \alpha_{w,Ref})$ as a function of axial position of measurement, where $\alpha_{w,Ref}$ is the results averaged in the range $x = 240D$ to $x = 250D$.

the wave travels with the mean flow velocity.

3.2 Mesh convergence study

A study of the spatial resolution was conducted on cases for horizontal flows with mean velocity $1.0\,\mathrm{m/s}$ and $1.5\,\mathrm{m/s}$ using water-cuts $25\,\%$, $50\,\%$ and $75\,\%$ as well as upwards inclined flows angled $1°$ and $5°$ at $1\,\mathrm{m/s}$ mean velocity and $50\,\%$ water-cut.

For the horizontal flow at $1.0\,\mathrm{m/s}$ with $50\,\%$ water-cut, four mesh sizes are tested, $\hat{\delta} \in [0.4, 0.2, 0.1, 0.05]$. The results are shown in Figure 6. It is seen that the y-position at which the first oil is observed converges towards the experimental observations, whereas the gradient of the volume fraction converges towards a slightly over-predicted dispersion. Near the bottom and top of the pipe ($2y/D = -1$ and $2y/D = 1$) the experimental results are not accurate and the deviations ignored (Kumara et al. 2009). Observed deviations in the experimental data suggests that the deviations lie within the expected uncertainty.

With increasing flow velocity the phases disperse more. Similarly to the slower flow, the simulation run at $1.5\,\mathrm{m/s}$ mean velocity shown in Figure 7 yields convergence towards a result slightly more dispersed than the experimental. On the contrary, at $75\,\%$ water-cut the model does not seem to converge within the mesh sizes and seems to under-predict the level of dispersion.

As the pipe is inclined transition to a wavy flow is expected where the time average would yield higher dispersion. For the upwards inclined flow (Figure 9) at $5°$, similar convergence as for the horizontal flows is observed.

Notably all the flow converges at around $\hat{\delta} = 0.1$. A deviation from the experimental observation is noticed, consistently predicting too high dispersion.
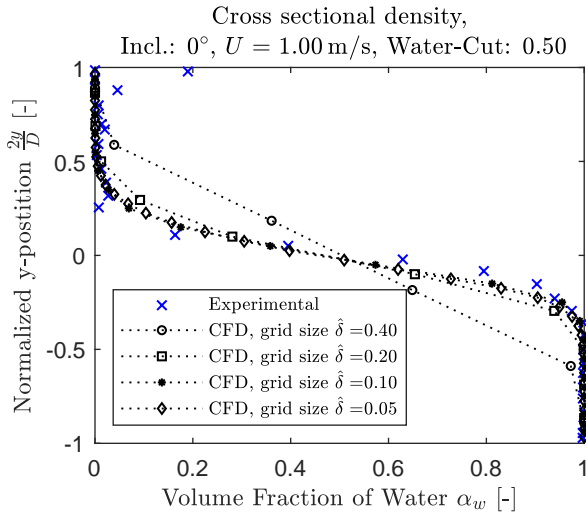
Figure 6: Mesh convergence study showing 4 successively decrementing grid sizes. Horizontal flow, Mean velocity: $1.0 \, \mathrm{m/s}$, Water-cut: $50 \, \%$. Experimental reference by (Kumara et al. 2009).
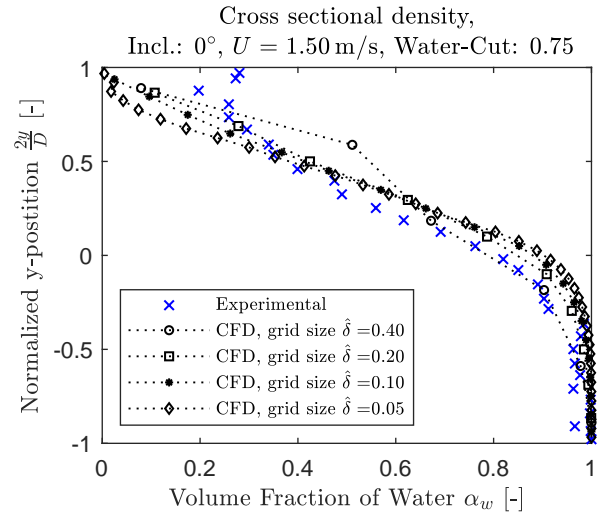

Figure 8: Mesh convergence study showing 4 successively decrementing grid sizes. Horizontal flow, Mean velocity: $1.5 \, \mathrm{m/s}$, Water-cut: $75 \, \%$. Experimental reference by (Kumara et al. 2009).
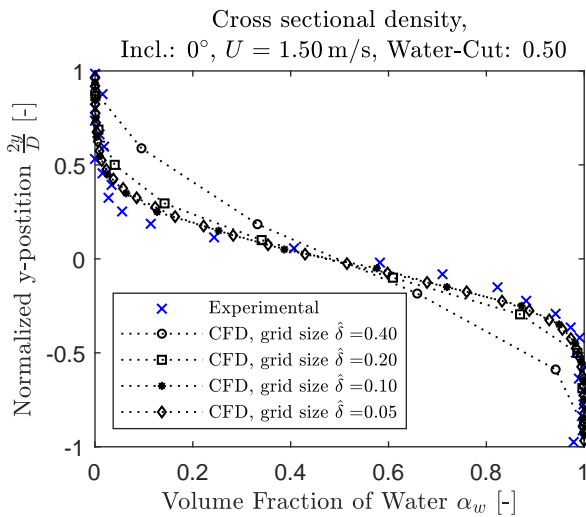

Figure 7: Mesh convergence study showing 4 successively decrementing grid sizes. Horizontal flow, Mean velocity: $1.5 \, \mathrm{m/s}$, Water-cut: $50 \, \%$. Experimental reference by (Kumara et al. 2009).

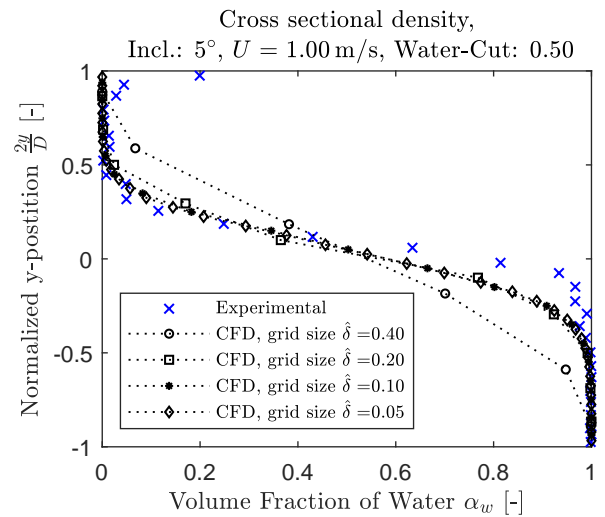**Figure 9:** Mesh convergence study showing 4 successively decrementing grid sizes. $5°$ upward inclined flow, Mean velocity: $1.0 \, \mathrm{m/s}$, Water-cut: $50 \, \%$. Experimental reference by (Kumara et al. 2009).

Cross sectional density,
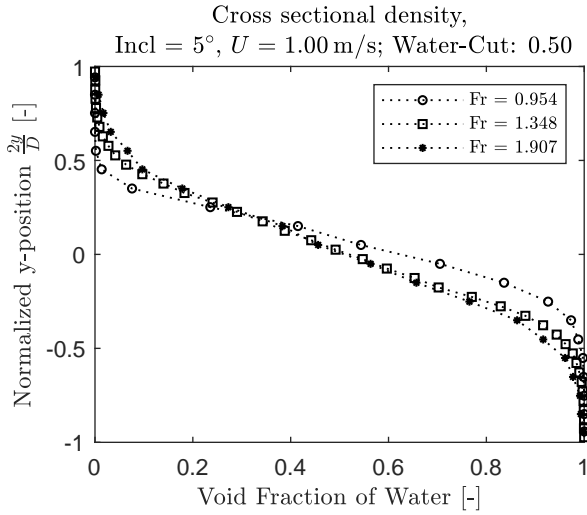Incl = 5°, $U = 1.00$ m/s; Water-Cut: 0.50

Figure 10: Cross sectional density plot for variation of the Froude number. Mean velocity: 1.0 m/s, Inclination: 5°, Re: 37684, A: 0.117, We: 1166.

3.3 Water-wetting, liquid holdup and dispersion

A study is performed on quantification of water-wetting along with estimation of liquid holdup and dispersion. For this study, a grid size of $\hat{\delta} = 0.1$ is used and the analysis data is extracted from a pipe section between $x = 55D$ and $x = 60D$. The models are run at 5° inclination with 1.0 m/s mean velocity and 50 % water-cut

The effect of the Froude number is simulated using three different gravitational constants, thereby keeping all other flow parameters constant. The resulting variations of the liquid holdup and water wetting are listed in Table 3. It is seen that the liquid holdup decreases for increasing Froude numbers as the effect of difference in densities is reduced. At the same time the water-wetting increases slightly. This can be described by a higher dispersion. This is shown in the density-plot in Figure 10, where it is seen that the rate of dispersion increases with the Froude number. This behaviour is supported by the assumption described in Section 2.10.

The density difference characterized through the Atwood number is analysed while keeping the mean density and thus the rest of the flow properties constant. The results are listed in Table 4 and shown as cross sectional density plots in Figure 11. Here, the increase of the Atwood number shows a larger liquid holdup with a lower dispersion. The water-wetting remains roughly constant.

Fr	Water-cut	Liquid holdup	Water-wetting
0.954	50 %	53.5 %	54.1 %
1.348	50 %	51.4 %	54.0 %
1.907	50 %	51.0 %	55.1 %

Table 3: Variation of the Froude number. Mean velocity: 1.0 m/s, Inclination: 5°, Re: 37684, A: 0.117, We: 1166.

A	Water-cut	Liquid holdup	Water-wetting
0.100	50 %	51.8 %	54.3 %
0.117	50 %	51.4 %	54.0 %
0.135	50 %	52.6 %	54.1 %

Table 4: Variation of the Atwood number. Mean velocity: 1.0 m/s, Inclination: 5°, Re: 37684, Fr: 1.348, We: 1166.

Cross sectional density,
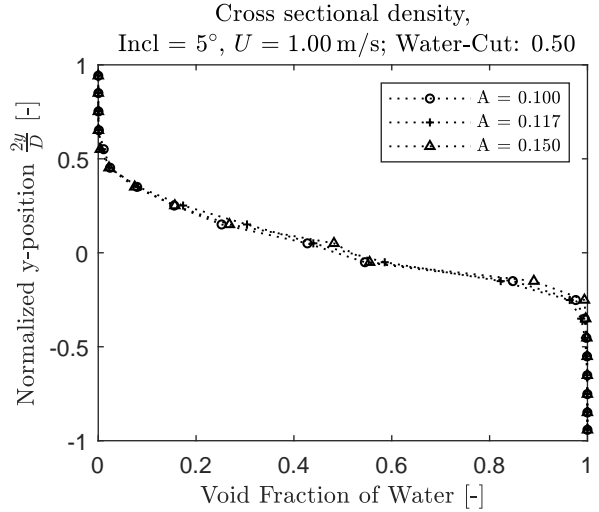Incl = 5°, $U = 1.00$ m/s; Water-Cut: 0.50

Figure 11: Cross sectional density plot for variation of the Atwood number. Mean velocity: 1.0 m/s, Inclination: 5°, Re: 37684, Fr: 1.348, We: 1166.

Conclusions

The present study has employed a CFD model to capture the flow patterns and phase distribution in a two-phase oil and water flow. The model has been refined and validated against experimental data with mean flow velocity of 1.0 m/s and 1.5 m/s and water-cuts 50 % and 75 %. Here the model shows good convergence towards the experimental data in terms of phase distribution. The physics causing the phase distribution are decomposed into dispersion and liquid holdup. This is used to analyse surface wetting for a set of Atwood and Froude numbers. The results shows how the Atwood number balances dispersion to liquid holdup having a rather constant water-wetting whereas the water-wetting increases with the Froude number although the liquid holdup is reduced. The variation of the Atwood number seems to have only marginally effect on the presented flow case.

References

Panagiota Angeli and Geoffrey F. Hewitt. Drop size distributions in horizontal oil-water dispersed flows. *Chem. Eng. Sci.*, 55(16):3133–3143, 2000.

J. U. Brackbill, D. B. Kothe, and C. Zemach. A continuum method for modeling surface tension. *J. Comput. Phys.*, 100 (2):335–354, 1992.

Neima Brauner. The prediction of dispersed flows boundaries

in liquid–liquid and gas–liquid systems. *Int. J. Multiphase Flow.*, 27(5):885–910, 2001.

Ronaldo G. dos Santos, Rahoma S. Mohamed, Antonio C. Bannwart, and Watson Loh. Contact angle measurements and wetting behavior of inner surfaces of pipelines exposed to heavy crude oil and water. *J. Petro. Sci. Engng.*, 51:9–16, 2006.

G. Elseth. *An experimental study of oil / water flow in horizontal pipes*. PhD thesis, Telemark University College, June 2001.

J. Glimm, J. W. Grove, X. L. Li, W. Oh, and D. H. Sharp. A critical analysis of Rayleigh-Taylor growth rates. *J. Comput. Phys.*, 169(2):652–677, 2001.

C. W. Hirt and B. D. Nichols. Volume of fluid (Vof) method for the dynamics of free boundaries. *J. Comput. Phys.*, 39(1): 201–225, 1981.

M. Ishii and T. Hibiki. *Thermo-fluid dynamics of two-phase flow*. Springer, 2nd edition, 2006.

W. A. S. Kumara, G. Elseth, B. M. Halvorsen, and M. C. Melaaen. Computational study of stratified two phase oil/water flow in horizontal pipes. In *HEFAT 2008*. Citeseer, June 2008.

W. A. S. Kumara, B. M. Halvorsen, and M. C. Melaaen. Pressure drop, flow pattern and local water volume fraction measurements of oil–water flow in pipes. *Meas. Sci. Technol.*, 20:114004, 2009.

Simon Lo and Dongsheng Zhang. Modelling of break-up and coalescence in bubbly two-phase flows. *Int. Comm. Heat Mass Transfer*, 1(1):23–38, 2009.

Hassan Pouraria, Jung Kwan Seo, and Jeom Kee Paik. A numerical study on water wetting associated with the internal corrosion of oil pipelines. *Ocean Engng.*, 122:105–117, 2016.

A. Prosperetti and G. Tryggvason. *Computational methods for multiphase flow*. Cambridge University Press, 2007.

L. Schiller and A. Naumann. Über die grundlegende berechnungen bei der schwerkraftaufbreitung. *Z. Ver. Deutsch. Ing.*, 77(12):318–320, 1933.

Heiner Schümann, Milad Khatibi, Murat Tutkun, Bjørnar H. Pettersen, Zhilin Yang, and Ole Jorgen Nydal. Droplet size measurements in oil–water dispersions: A comparison study using FBRM and PVM. *J. Disp. Sci. Tech.*, 36(10):1432–1443, 2015.

Tsan-Hsing Shih, William W. Liou, Aamir Shabbir, Zhigang Yang, and Jiang Zhu. A new k-ϵ eddy viscosity model for high Reynolds number turbulent flows. *Computers & Fluids*, 24(3):227–238, 1995.

L. Strubelj, I. Tiselj, and B. Mavko. Simulations of free surface flows with implementation of surface tension and interface sharpening in the two-fluid model. *Int. J. Heat Fluid Flow*, 30(4):741–750, 2009.

G. T. Taylor. The instability of liquid surfaces when accelerated in a direction perpendicuar to their planes. *Proc. R. Soc. Lond.*, 201:192–196, 1950.